Fourier modal method for moiré lattices

Natalia S. Salakhova and Ilia M. Fradkin [*]

Skolkovo Institute of Science and Technology, Bolshoy Boulevard 30, Building 1, Moscow 121205, Russia
and Moscow Institute of Physics and Technology, Institutskiy pereulok 9, Moscow Region 141701, Russia

Sergey A. Dyakov and Nikolay A. Gippius

Skolkovo Institute of Science and Technology, Bolshoy Boulevard 30, Building 1, Moscow 121205, Russia

In recent years twisted bilayers of two-dimensional (2D) materials have become very popular in the field due to the possibility to totally change their electronic properties by simple rotation. At the same time, in the wide field of photonic crystals, this idea still remains almost untouched, and only some particular problems have been considered. One of the reasons is the computational difficulty of accurate consideration of moiré superlattices that appear due to the superimposition of misaligned lattices. Indeed, the unit cell of the complex lattice is typically much larger than the original crystals and requires many more computational resources for the computations. Here, we propose a moiré-adapted Fourier modal method (MA-FMM) in the form of scattering matrices for the description of twisted one-dimensional (1D) gratings' stacks. We demonstrate that MA-FMM allows us to consider sublattices in close vicinity to each other and account for their interaction via the near field. In the developed numerical scheme, we utilize the fact that each sublattice is only 1D periodic and therefore simpler than the resulting 2D superlattice, as well as the fact that even a small gap between the lattices filters out high Fourier harmonics due to their evanescent origin. Such approach accelerates the computations from 1 up to 3 or more orders of magnitude for typical structures depending on the number of harmonics. In turn, the high computational speed paves the way for rigorous study of almost any photonic crystals of the proposed geometry and demonstration of specific moiré-associated effects.

I. INTRODUCTION

The moiré effect, known for centuries, is a result of superimposing similar but misaligned lattices. Probably, everyone has seen moiré fringes as an occasional effect (recognizable patterns on silk clothes and curtains) or as a side effect (prominent grids on photos of LCD screens and computational-grid-assisted artefacts on map graphs), but the most important effects are their practical applications. For example, the moiré pattern underlies the widely known Vernier scale, which is implemented in micrometers and other measuring devices. Also, the moiré effect has been successfully applied in strain analysis [1–3], optical alignment [4–7], medicine [8], biosensors [9–11], the detection of document counterfeiting [12–15], and many other spheres [16,17]. Nevertheless, the original principle of the complex superlattice design by the superimposition of identical or similar sublattices is still widely applied to observe the associated phenomena. In the last few years, there has been a breakthrough in the field of twisting two-dimensional (2D) materials. The possibility to observe superconductivity [18–20], ferromagnetism [21–24], and other impressive effects [25–28] has been demonstrated just by the appropriate choice of the rotation angle between two layers. The obvious success attracted attention to moiré lattices and even led to the rise of the separate field of twistronics.

In this paper, we consider moiré patterns in the context of nanophotonic metasurfaces. All kinds of photonic crystals and metasurfaces have been studied intensively for the last several decades, and their optical properties are known in great detail. In recent years there has been a growth in attention to stacks of metasurfaces [29–38] due to the new opportunities that they provide for the control and manipulation of light. Simultaneously, many fewer studies have considered the interaction of crystals that do not have a mutual lattice because of either the period discrepancy or even misalignment of crystallographic axes. The rise of twistronics attracted deserved attention to this field and gave it a significant boost. As a result, currently, there are a number of studies available that demonstrate various effects in photonic moiré metasurfaces. Twisted stacks have been used to demonstrate topological transitions of the guided modes [39–45], light localization in moiré supercells [46–48], tunable metasurfaces [49], and chirality enhancement [49–51]. Also, it has been shown that in the near-field radiative heat transfer between parallel planar metasurfaces [52–57], the heat flux can be controlled by twisting one of the corrugated plates relative to the other [45,58–61]. Some of the studies utilize laser interference lithography to obtain stacks of large-area lattices [49] and single-layer, gradient moiré metasurfaces [16,62]. Nevertheless, the general understanding of the optical moiré physics and potential capabilities are still to be understood.

[*]Ilia.Fradkin@skoltech.ru

The available calculation approaches for predicting properties of such structures do not provide the full picture. Most papers have proposed either to apply an effective medium approximation [39] or to build a transfer/scattering matrix approach for the main (zeroth) diffraction channel [44,63–69], and only the most recent studies have suggested some advanced approaches [70–72]. The first two approaches undoubtedly boost and simplify the calculations but have strongly limited application area. The effective medium approximation typically describes very dense and thin metasurfaces, whereas the main diffraction order approximation requires a large distance between the sublattices to prevent their interaction via the evanescent waves forming the near field. In this way, none of the approaches allows considering the hybridization of typical quasiguided modes of twisted photonic structures, the backbone of plenty of physical systems. Universal computational methods such as the finite-element method (FEM), the finite-difference time domain (FDTD) method, and the Fourier modal method (FMM) [73], also known as the rigorous coupled-wave analysis method [74], are not efficient in the application of such structures. On the one hand, the unit cell of the moiré superlattice is larger (and often much larger) than the unit cells of the original gratings, which significantly complicates the real-space-based calculations (FEM, FDTD). On the other hand, a large unit cell corresponds to a small Bragg vector in reciprocal space, and in turn, a large number of Fourier harmonics have to be accounted for to reach the convergence of reciprocal-space-based FMM. Remarkably, the brightest twistronic effects are observed for identical materials rotated on very small angles [18,20–22,26], which corresponds to extremely large periods of the resulting superlattice. This configuration, together with nontwisted sublattices with very close periods, is the hardest-to-compute structure. Thus, there is great need for a fast and universal computational method specialized for considering stacks of twisted metasurfaces.

In this paper, we present the moiré-adapted Fourier modal method (MA-FMM) in the form of scattering matrices [73] to consider twisted stacks of one-dimensional (1D) periodic metasurfaces. Scattering matrices of each sublattice are calculated efficiently, accounting for their 1D-periodic origin, which makes the procedure efficient. To calculate the scattering matrix of the whole stack, we additionally propose to ignore high-$k_\parallel$ evanescent waves that decay in the gap-layer between sublattices in such a fast way that do not affect the coupling between them at all. Both procedures strongly boost the calculations without a noticeable loss of accuracy and pave the way to study the optical properties of the twisted stacks in a reasonable amount of time. To demonstrate the proposed approach performance, we compare its computation speed with the standard FMM and show acceleration of 1 to 3 or more orders of magnitude. Finally, we demonstrate the possible applications using examples of both plasmonic and dielectric twisted stacks. The plasmonic stack, which is one of the most difficult for computations, allows controlling the shape of the plasmon dispersion just by a relative rotation of the sublayers. We also show that the chiral diamond photonic crystal slab with inclusions of graphite is able to generate circularly polarized thermal emission (as well as to route the radiation from the circularly polarized emitter) for
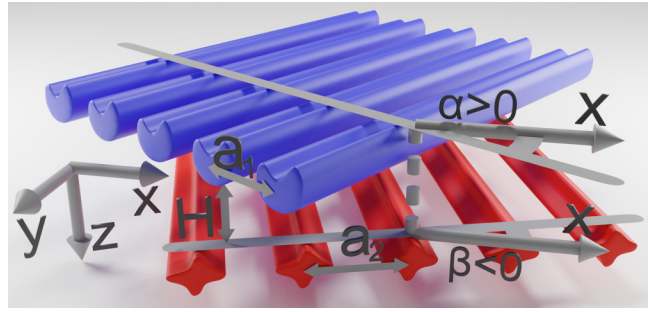

FIG. 1. Schematic of the twisted stack consisting of two arbitrary 1D-periodic lattices twisted around a common axis.

appropriate twisting angles. The accurate study of these and many other effects becomes possible with the help of our approach.

II. SCATTERING MATRICES CALCULATIONS

Here, we are going to consider twisted stacks of 1D-periodic gratings that form a 2D-periodic moiré pattern, as shown in Fig. 1. The upper and lower sublattices might be different and have different periods and arbitrary rotation angles, as depicted in Figs. 1 and 2.

Each separate 1D lattice has a corresponding 1D reciprocal lattice [Figs. 2(a) and 2(b)], which is formed by the Bragg vectors $\mathbf{G}^1$ and $\mathbf{G}^2$, which might be imparted by the lattices to the in-plane wave vector of the incident wave $\mathbf{k}_\parallel$. The optical properties of the upper and lower sublattices can be described in terms of the scattering matrices that connect the amplitudes of incoming and outgoing waves. Nevertheless, the relative rotation and different periods of the lattices result in misalignment and mismatch of their reciprocal lattices [see Figs. 2(a) and 2(b)]. In such configuration, each diffraction harmonic of the light passed through one of the lattices generates a new family of harmonics after the diffraction on the second one. Therefore, the structure consisting of upper and lower sublattices is essentially two-dimensional, and its scattering matrix should connect all the corresponding harmonics [see Fig. 2(c)].

The straightforward approach to calculate the spectra of such stacks is just to consider each 1D-periodic sublayer as a 2D-periodic metasurface [see the right column in Figs. 2(a) and 2(b)]. For the desired convergence, 2D structures typically require us to take into account many more harmonics than 1D ones. Given that the calculation time scales cubically with the number of harmonics [73], 2D calculations are relatively slow and resource consuming. The straightforward approach becomes especially inefficient for plasmonic lattices, for which even 1D sublattices require a huge number of harmonics to resolve the high-gradient fields. Brute-force calculation of such structures is challenging even in a single dimension and almost unachievable in two dimensions. Moreover, for moiré lattices, this issue might be even more critical than for typical 2D crystals. As already mentioned, the moiré pattern composed of sublayers with close vectors of reciprocal lattices $|\mathbf{G}^1 - \mathbf{G}^2| \ll k$ (where k is the typical wave vector of light in ambient media) has a large number of open diffraction
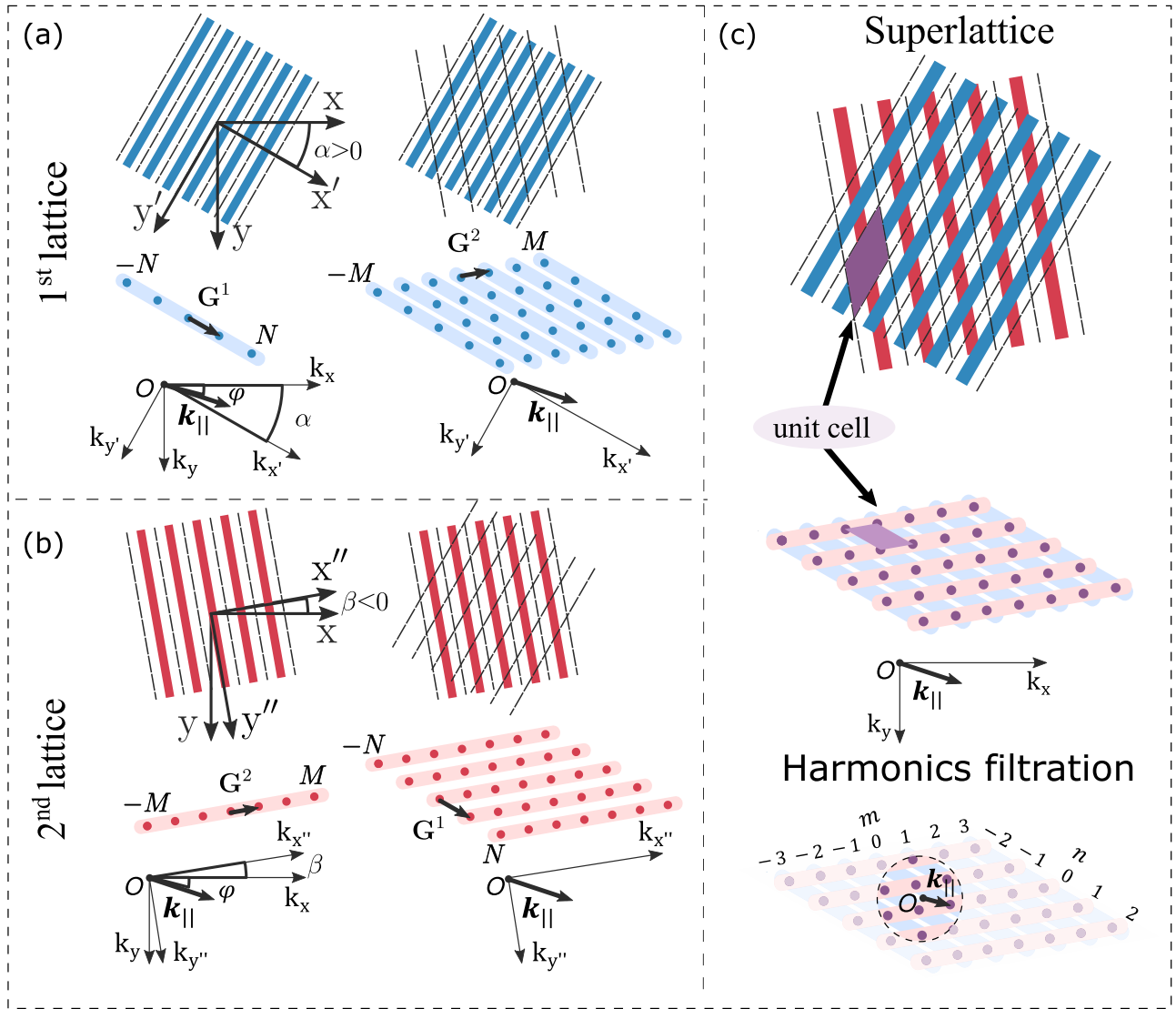
FIG. 2. Sketches of the (a) upper and (b) lower sublattices and (c) their stack in real and reciprocal spaces. The left column in (a) and (b) schematically shows the structure of the rotated 1D-periodic sublattices and their reciprocal lattices with respect to the coordinate axes and wave vector of the incident light $\mathbf{k}_\parallel$. The right column in (a) and (b) formally considers the same sublattices as structures with mutual 2D periodicity. Each sublattice binds harmonics of either a common row or column. (c) shows the superimposing of 1D sublattices resulting in the formation of the true 2D-periodic structure, which substantially connects all the harmonics. The dashed circle in the bottom plot contains the harmonics that fulfill condition (26) $|\mathbf{k}_\parallel + n\mathbf{G}^1 + m\mathbf{G}^2| < \sqrt{\varepsilon_{\mathrm{gl}}\omega^2/c^2 + (-\ln\Theta/H)^2}$ for real $\varepsilon_{\mathrm{gl}}$ and therefore are used for the calculation of twisted lattices coupling.

channels. Thus, in this case, the achievement of full convergence for some structures could be especially challenging, which will be discussed for a practical example below.

Nevertheless, we do not consider 2D photonic crystals of the general form and focus our attention on a rather narrow class of the structures. Using the distinctive features of this class makes it possible to simplify and boost the corresponding calculations.

A. Scattering matrix of the 1D lattice

We start with the consideration of the first (upper) 1D sublattice. It is important to note that the derivations will be based on the assumption that the lattice is sandwiched between two homogeneous layers (see Fig. 3). Such an environment makes

it possible to consider the eigenmodes of the boundary layers as plane linearly polarized waves, which simplifies the derivations. Although the proposed configuration does not describe the arbitrary structure, we can implement it without losing generality. Indeed, the virtual zero-thickness homogeneous layer can always be inserted, for example, between two back-to-back gratings.

Let us separate out the layer bounded by horizontal dashed lines [see Figs. 2(a) and 3] that includes the upper sublattice in a specially aligned x'-y' coordinate system. Looking ahead, a similar layer for the lower sublattice should be chosen to stand back to back with the first one; that is, the gap interlayer is virtually divided in an arbitrary ratio between the layers. Incident light determines the in-plane components of the main harmonic wave vector $\mathbf{k}_\parallel = k_x\hat{x} + k_y\hat{y} = k_{x'}\hat{x}' + k_{y'}\hat{y}'$, where
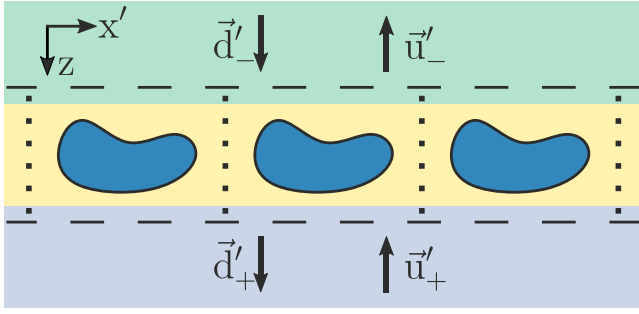
FIG. 3. Scheme of the 1D lattice sandwiched between homogeneous adjacent layers. Long-dashed lines separate the periodic part of the structure from the outer dielectric environment and lie in homogeneous layers; short-dashed lines denote the boundaries of the unit cells. Arrows illustrate the incoming and outgoing harmonics that are connected via the scattering matrix.

$\hat{x}$, $\hat{y}$, $\hat{x}'$, and $\hat{y}'$ are unit vectors defining the direction of the corresponding axes. The interaction of light with the lattice leads to the emergence of diffraction harmonics that have corresponding wave vectors that might be arranged in hypervectors:

$$
\begin{bmatrix} \vec{K}_{x'}^1 & \vec{K}_{y'}^1 \end{bmatrix} = \begin{bmatrix} K_{x'}^{1,-N} & K_{y'}^{1,-N} \\ K_{x'}^{1,-N+1} & K_{y'}^{1,-N+1} \\ \vdots & \\ K_{x'}^{1,0} & K_{y'}^{1,0} \\ \vdots & \\ K_{x'}^{1,N} & K_{y'}^{1,N} \end{bmatrix}
$$

$$
= \begin{bmatrix} 1 \\ 1 \\ \vdots \\ 1 \\ \vdots \\ 1 \end{bmatrix} \begin{bmatrix} k_{x'} \\ k_{y'} \end{bmatrix}^T + \begin{bmatrix} -N \\ -N+1 \\ \vdots \\ 0 \\ \vdots \\ N \end{bmatrix} \begin{bmatrix} G_{x'}^1 \\ G_{y'}^1 \end{bmatrix}^T, \quad (1)
$$

where $G_{x'}^1$ and $G_{y'}^1$ are projections of the Bragg vector on the denoted axes and the number of harmonics that are taken into account is $N_g = 2N + 1$. The finite number of these harmonics makes it possible to build the scattering matrix that connects the amplitudes of incoming $[\vec{d}_-', \vec{u}_+']^T$ and outgoing $[\vec{d}_+', \vec{u}_-']^T$ waves on the boundaries of the considered layer (horizontal dashed lines in Fig. 3). Since the consideration is held in the primed basis, we consider the matrix $\mathbb{S}_1'(\omega, \mathbf{k}_\parallel) = \mathbb{S}_1'(\omega, [k_{x'}, k_{y'}]^T)$ as a function of $k_{x'}$ and $k_{y'}$ projections:

$$
\begin{bmatrix} \vec{d}_+' \\ \vec{u}_-' \end{bmatrix} = \mathbb{S}_1'(\omega, [k_{x'}, k_{y'}]^T) \begin{bmatrix} \vec{d}_-' \\ \vec{u}_+' \end{bmatrix}, \quad (2)
$$

where $\vec{u}_\pm'$ and $\vec{d}_\pm'$ are hypervectors of amplitudes corresponding to the upward and downward propagating waves and $+$ and $-$ signs indicate the sections that have the larger and smaller z coordinates, correspondingly. Each of the hypervectors $\vec{u}_\pm'$, $\vec{d}_\pm'$ describes $2N_g$ modes of different polarizations, whereas the scattering matrix $\mathbb{S}_1'$ has a size of $4N_g \times 4N_g$. If the boundaries of the considered layer are located inside a homogeneous environment (the case which we consider here),

then according to our definition, amplitudes correspond to x'- and y'-polarized plane waves:

$$
\vec{u}_\pm' = \begin{bmatrix} \vec{u}_{\pm,x'} \\ \vec{u}_{\pm,y'} \end{bmatrix}, \quad \vec{d}_\pm' = \begin{bmatrix} \vec{d}_{\pm,x'} \\ \vec{d}_{\pm,y'} \end{bmatrix}, \quad (3)
$$

where the amplitudes are sorted in accordance with hypervectors $[\vec{K}_{x'}^1, \vec{K}_{y'}^1]$ in such a way that the field of up- and downgoing waves can be found as follows:

$$
\begin{bmatrix} E_{\pm,x'}(\mathbf{r}_\parallel) \\ E_{\pm,y'}(\mathbf{r}_\parallel) \end{bmatrix} = \sum_{n=-N}^{N} \left(\begin{bmatrix} u_{\pm,x'}^n \\ u_{\pm,y'}^n \end{bmatrix} + \begin{bmatrix} d_{\pm,x'}^n \\ d_{\pm,y'}^n \end{bmatrix} \right) e^{i\mathbf{K}_\parallel^{1,n} \mathbf{r}_\parallel}, \quad (4)
$$

where index n indicates the nth component of the hypervectors, $\mathbf{K}_\parallel^{1,n} = K_x^{1,n} \hat{x} + K_y^{1,n} \hat{y}$ and $\mathbf{r}_\parallel = x\hat{x} + y\hat{y}$.

B. Scattering matrix of the rotated sublattice

The scattering matrix $\mathbb{S}_1'$ fully describes the optical properties of the considered layer and can be found with standard FMM realizations. This matrix is a function of frequency ω and the in-plane component of the wave vector $\mathbf{k}_\parallel$ but also depends on the structure's parameters. The scattering matrix's transformation with the rotation of the lattice can be easily found and does not require additional computations. To demonstrate this, we consider the first lattice rotated by an angle α and find the connection of the scattering matrix in the x-y coordinate system $\mathbb{S}_1(\omega, \mathbf{k}_\parallel) = \mathbb{S}_1(\omega, [k_x, k_y]^T)$ with matrix $\mathbb{S}_1'(\omega, \mathbf{k}_\parallel) = \mathbb{S}_1'(\omega, [k_{x'}, k_{y'}]^T)$ defined in the x'-y' basis [see Fig. 2(a)]. The latter has already been considered:

$$
\begin{bmatrix} d_{+,x'} \\ d_{+,y'} \\ u_{-,x'} \\ u_{-,y'} \end{bmatrix} = \mathbb{S}_1'\left(\omega, [k_{x'}, k_{y'}]^T\right) \begin{bmatrix} d_{-,x'} \\ d_{-,y'} \\ u_{+,x'} \\ u_{+,y'} \end{bmatrix}. \quad (5)
$$

Hypervectors that are connected by the scattering matrix might be easily expressed in the original x-y coordinate system:

$$
\begin{bmatrix} d_{+,x} \\ d_{+,y} \\ u_{-,x} \\ u_{-,y} \end{bmatrix} = \mathbb{R}_\alpha \begin{bmatrix} d_{+,x'} \\ d_{+,y'} \\ u_{-,x'} \\ u_{-,y'} \end{bmatrix}, \quad \begin{bmatrix} d_{-,x} \\ d_{-,y} \\ u_{+,x} \\ u_{+,y} \end{bmatrix} = \mathbb{R}_\alpha \begin{bmatrix} d_{-,x'} \\ d_{-,y'} \\ u_{+,x'} \\ u_{+,y'} \end{bmatrix},
$$

$$
\mathbb{R}_\alpha = \begin{bmatrix} \cos(\alpha)\hat{I} & -\sin(\alpha)\hat{I} & \hat{0} & \hat{0} \\ \sin(\alpha)\hat{I} & \cos(\alpha)\hat{I} & \hat{0} & \hat{0} \\ \hat{0} & \hat{0} & \cos(\alpha)\hat{I} & -\sin(\alpha)\hat{I} \\ \hat{0} & \hat{0} & \sin(\alpha)\hat{I} & \cos(\alpha)\hat{I} \end{bmatrix}, \quad (6)
$$

where $\mathbb{R}_\alpha$ is the rotation matrix of the hypervectors, $\hat{I}$ is the $N_g \times N_g$ identity matrix, and $\hat{0}$ is the $N_g \times N_g$ zero matrix. Due to the fact that both scattering matrices describe the same mapping in different bases, we can easily obtain the final expression for the scattering matrix in the original coordinates:

$$
\mathbb{S}_1(\omega, [k_x, k_y]^T) = \mathbb{R}_\alpha \mathbb{S}_1'(\omega, \hat{R}_{-\alpha}[k_x, k_y]^T) \mathbb{R}_{-\alpha}, \quad (7)
$$

where

$$
\begin{bmatrix} k_{x'} \\ k_{y'} \end{bmatrix} = \hat{R}_{-\alpha} \begin{bmatrix} k_x \\ k_y \end{bmatrix}, \quad \hat{R}_\alpha = \begin{bmatrix} \cos(\alpha) & -\sin(\alpha) \\ \sin(\alpha) & \cos(\alpha) \end{bmatrix}. \quad (8)
$$

We should remember that the in-plane components of the wave vectors of the diffraction harmonics, $\mathbf{K}_\parallel^{1,n} = K_x^{1,n} \hat{x} +$

$K_y^{1,n}\hat{y} = K_{x'}^{1,n}\hat{x}' + K_{y'}^{1,n}\hat{y}'$, are transformed accordingly:

$$\begin{bmatrix} K_x^{1,n}(\mathbf{k}_\parallel) \\ K_y^{1,n}(\mathbf{k}_\parallel) \end{bmatrix} = \begin{bmatrix} k_x \\ k_y \end{bmatrix} + n \begin{bmatrix} G_x^1 \\ G_y^1 \end{bmatrix}$$

$$= \hat{R}_\alpha \begin{bmatrix} K_{x'}^{1,n}(\mathbf{k}_\parallel) \\ K_{y'}^{1,n}(\mathbf{k}_\parallel) \end{bmatrix} = \hat{R}_\alpha \begin{bmatrix} k_{x'} \\ k_{y'} \end{bmatrix} + n\hat{R}_\alpha \begin{bmatrix} G^1 \\ 0 \end{bmatrix}, \quad (9)$$

where G^1 is the absolute value of the Bragg vector of the first lattice ($G^1 = G_{x'}^1 = \sqrt{G_x^{1\,2} + G_y^{1\,2}}$).

The same procedure holds for the second lattice, which is rotated on an angle β and is aligned with the double-primed axes:

$$\mathbb{S}_2(\omega, [k_x, k_y]^\mathrm{T}) = \mathbb{R}_\beta \mathbb{S}_2''(\omega, \hat{R}_{-\beta}[k_x, k_y]^\mathrm{T})\mathbb{R}_{-\beta}. \quad (10)$$

The corresponding basis is as follows:

$$\begin{bmatrix} K_x^{2,m}(\mathbf{k}_\parallel) \\ K_y^{2,m}(\mathbf{k}_\parallel) \end{bmatrix} = \begin{bmatrix} k_x \\ k_y \end{bmatrix} + m \begin{bmatrix} G_x^2 \\ G_y^2 \end{bmatrix} = \hat{R}_\beta \begin{bmatrix} k_{x''} \\ k_{y''} \end{bmatrix} + m\hat{R}_\beta \begin{bmatrix} G^2 \\ 0 \end{bmatrix}. \quad (11)$$

The number of harmonics for this case is denoted $M_g = 2M + 1$.

C. Scattering matrix of the stack in the mutual basis

We have obtained the scattering matrices of the rotated 1D metasurfaces, but our final goal is to construct the scattering matrices derived in a mutual basis, which requires us to consider them formally as 2D crystals. The mutual, reciprocal lattice for both sublattices might be found as the direct sum of their own 1D reciprocal lattices. In practical calculations, we take into account only a finite number of harmonics, and the easiest approach is also to take the direct sum of finite sublattices, as shown in the right column in Figs. 2(a) and 2(b). Such an approach is not the only one, but it is highly convenient for practical implementation.

The wave vectors of the 2D superlattice harmonics might be arranged in a single hypervector in different orders. The straightforward approach is to place wave vectors of the 2D lattice "row" after "row" or "column" after "column." In other words, harmonics of the mutual basis can be constructed as a concatenation of sets of harmonics of 1D lattices for different wave vectors of the main harmonic.

For the consideration of the first (upper) lattice, it is convenient to arrange the wave vectors in the order, which we indicate by the letter A [see the right column of Figs. 2(a) and 2(b)]:

$$\begin{bmatrix} ^\mathrm{A}\vec{K}_x^{2\mathrm{D}} & ^\mathrm{A}\vec{K}_y^{2\mathrm{D}} \end{bmatrix}$$

$$= \begin{bmatrix} \vec{K}_x^1(\mathbf{k}_\parallel - M\mathbf{G}^2) & \vec{K}_y^1(\mathbf{k}_\parallel - M\mathbf{G}^2) \\ \vec{K}_x^1(\mathbf{k}_\parallel + (-M+1)\mathbf{G}^2) & \vec{K}_y^1(\mathbf{k}_\parallel + (-M+1)\mathbf{G}^2) \\ \vdots & \vdots \\ \vec{K}_x^1(\mathbf{k}_\parallel + M\mathbf{G}^2) & \vec{K}_y^1(\mathbf{k}_\parallel + M\mathbf{G}^2) \end{bmatrix}$$

$$= \begin{bmatrix} \vec{K}_x^1(\mathbf{K}_\parallel^{2,-M}[\mathbf{k}_\parallel]) & \vec{K}_y^1(\mathbf{K}_\parallel^{2,-M}[\mathbf{k}_\parallel]) \\ \vec{K}_x^1(\mathbf{K}_\parallel^{2,-M+1}[\mathbf{k}_\parallel]) & \vec{K}_y^1(\mathbf{K}_\parallel^{2,-M+1}[\mathbf{k}_\parallel]) \\ \vdots & \vdots \\ \vec{K}_x^1(\mathbf{K}_\parallel^{2,M}[\mathbf{k}_\parallel]) & \vec{K}_y^1(\mathbf{K}_\parallel^{2,M}[\mathbf{k}_\parallel]) \end{bmatrix}, \quad (12)$$

where the expression $\vec{K}_{x/y}^1(\mathbf{q})$ indicates that the corresponding hypervector is calculated for the wave vector of the main harmonic equal to $\mathbf{q}$.

With such a choice of the basis, each block of the scattering matrix of the first lattice (considered a 2D one) splits into subblocks that describe the internal coupling of each row's harmonics. Since the lattice is fundamentally one-dimensional, all the interrow connections are equal to zero, which makes the scattering matrix $^\mathrm{A}\mathcal{S}_1$ of the first lattice formally considered a 2D crystal sparse. To demonstrate this, we first represent the scattering matrices in the form in which each block is responsible for either reflection or transmission of x- or y-polarized incident light to the x- or y-polarized channels:

$$^\mathrm{A}\mathcal{S}_1(\omega, \mathbf{k}_\parallel) = \begin{pmatrix} ^\mathrm{A}\mathcal{S}_1^{11} & ^\mathrm{A}\mathcal{S}_1^{12} & ^\mathrm{A}\mathcal{S}_1^{13} & ^\mathrm{A}\mathcal{S}_1^{14} \\ ^\mathrm{A}\mathcal{S}_1^{21} & ^\mathrm{A}\mathcal{S}_1^{22} & ^\mathrm{A}\mathcal{S}_1^{23} & ^\mathrm{A}\mathcal{S}_1^{24} \\ ^\mathrm{A}\mathcal{S}_1^{31} & ^\mathrm{A}\mathcal{S}_1^{32} & ^\mathrm{A}\mathcal{S}_1^{33} & ^\mathrm{A}\mathcal{S}_1^{34} \\ ^\mathrm{A}\mathcal{S}_1^{41} & ^\mathrm{A}\mathcal{S}_1^{42} & ^\mathrm{A}\mathcal{S}_1^{43} & ^\mathrm{A}\mathcal{S}_1^{44} \end{pmatrix},$$

$$\mathbb{S}_1(\omega, \mathbf{k}_\parallel) = \begin{pmatrix} \mathbb{S}_1^{11} & \mathbb{S}_1^{12} & \mathbb{S}_1^{13} & \mathbb{S}_1^{14} \\ \mathbb{S}_1^{21} & \mathbb{S}_1^{22} & \mathbb{S}_1^{23} & \mathbb{S}_1^{24} \\ \mathbb{S}_1^{31} & \mathbb{S}_1^{32} & \mathbb{S}_1^{33} & \mathbb{S}_1^{34} \\ \mathbb{S}_1^{41} & \mathbb{S}_1^{42} & \mathbb{S}_1^{43} & \mathbb{S}_1^{44} \end{pmatrix}, \quad (13)$$

where blocks $^\mathrm{A}\mathcal{S}_1^{ij}$ are size $N_g M_g \times N_g M_g$, whereas blocks $\mathbb{S}_1^{ij}$ are size $N_g \times N_g$. In turn, the blocks are obviously connected as follows:

$$^\mathrm{A}\mathcal{S}_1^{ij}(\omega, \mathbf{k}_\parallel) = \begin{pmatrix} \mathbb{S}_1^{ij}(\mathbf{K}_\parallel^{2,-M}[\mathbf{k}_\parallel]) & \hat{0} & \dots & \hat{0} \\ \hat{0} & \mathbb{S}_1^{ij}(\mathbf{K}_\parallel^{2,-M+1}[\mathbf{k}_\parallel]) & \dots & \hat{0} \\ \vdots & \vdots & \ddots & \vdots \\ \hat{0} & \hat{0} & \dots & \mathbb{S}_1^{ij}(\mathbf{K}_\parallel^{2,M}[\mathbf{k}_\parallel]) \end{pmatrix}. \quad (14)$$

Next, we need to build the scattering matrix of the second lattice $^\mathrm{A}\mathcal{S}_2$ in the same basis, A. However, it is hard to do it immediately, and therefore, we first consider the scattering matrix of the second lattice in its natural basis, denoted B [see the "chains" in the right column of Fig. 2(b)]:

$$^\mathrm{B}\mathcal{S}_2^{ij}(\omega, \mathbf{k}_\parallel) = \begin{pmatrix} \mathbb{S}_2^{ij}(\mathbf{K}_\parallel^{1,-N}[\mathbf{k}_\parallel]) & \hat{0} & \dots & \hat{0} \\ \hat{0} & \mathbb{S}_2^{ij}(\mathbf{K}_\parallel^{1,-N+1}[\mathbf{k}_\parallel]) & \dots & \hat{0} \\ \vdots & \vdots & \ddots & \vdots \\ \hat{0} & \hat{0} & \dots & \mathbb{S}_2^{ij}(\mathbf{K}_\parallel^{1,N}[\mathbf{k}_\parallel]) \end{pmatrix}, \quad (15)$$

where the harmonics are sorted as follows:

$$
\begin{bmatrix} {}^{\mathrm{B}}\vec{K}_x^{\mathrm{2D}} & {}^{\mathrm{B}}\vec{K}_y^{\mathrm{2D}} \end{bmatrix}
$$

$$
= \begin{bmatrix}
\vec{K}_x^2(\mathbf{K}_\parallel^{1,-N}[\mathbf{k}_\parallel]) & \vec{K}_y^2(\mathbf{K}_\parallel^{1,-N}[\mathbf{k}_\parallel]) \\
\vec{K}_x^2(\mathbf{K}_\parallel^{1,-N+1}[\mathbf{k}_\parallel]) & \vec{K}_y^2(\mathbf{K}_\parallel^{1,-N+1}[\mathbf{k}_\parallel]) \\
\vdots & \vdots \\
\vec{K}_x^2(\mathbf{K}_\parallel^{1,N}[\mathbf{k}_\parallel]) & \vec{K}_y^2(\mathbf{K}_\parallel^{1,N}[\mathbf{k}_\parallel])
\end{bmatrix}. \quad (16)
$$

The blockwise computation of the matrices (similar to [70]) is faster than a straightforward approach. Indeed, the calculation time of each scattering matrix scales cubically with the number of harmonics. Therefore, the straightforward consideration of each sublayer as 2D crystal takes $\tau_{\mathrm{sf}} \propto N_g^3 M_g^3$, whereas our blockwise-calculation approach for the first and second lattices scales as $\tau_1 \propto N_g^3 M_g$ and $\tau_2 \propto N_g M_g^3$, which is much faster in practice, especially for the large number of harmonics.

The knowledge of the ${}^{\mathrm{A}}\mathcal{S}_1(\omega, \mathbf{k}_\parallel)$ and ${}^{\mathrm{B}}\mathcal{S}_2(\omega, \mathbf{k}_\parallel)$ matrices is still not enough to obtain the stack scattering matrix. To do that, we need to consider matrices of both sublayers in a mutual basis. In our case, bases A and B differ only by the order of their elements, and therefore, one of them can be reduced to another by simple rearrangement. The transition matrix that connects them can be easily derived.

Indeed, when we consider basis A, the (n, m) harmonic [see Fig. 2(a)] has index number $p_{\mathrm{A}} = (m + M)N_g + n + N + 1$. The same harmonic in basis B [see Fig. 2(b)] has index number $p_{\mathrm{B}} = (n + N)M_g + m + M + 1$. In these terms the matrices in the A and B representations are connected in a very simple way:

$$
{}^{\mathrm{A}}\mathcal{S}_{2,p_{\mathrm{A}}q_{\mathrm{A}}}^{ij} = {}^{\mathrm{B}}\mathcal{S}_{2,p_{\mathrm{B}}q_{\mathrm{B}}}^{ij}, \quad (17)
$$

where indices ij indicate one of 16 blocks [see Eq. (13)] and the indices $p_{\mathrm{A/B}}q_{\mathrm{A/B}}$ run inside each of the blocks.

In practice, there are several possible ways to implement the described permutation. The most obvious is just to iterate over all the indices in a loop to find the scattering matrix components. Nevertheless, a much more effective approach is to build the mappings $p_{\mathrm{A}} = T_{\mathrm{AB}}(p_{\mathrm{B}})$ and $p_{\mathrm{B}} = T_{\mathrm{BA}}(p_{\mathrm{A}})$ between the representations in advance and apply them on demand. T_{AB} and T_{BA} are primitive functions tabulated according to the described rule. In this way, we need to apply just the permutation operation, which is available in most packages for numerical computations:

$$
{}^{\mathrm{A}}\mathcal{S}_{2,p_{\mathrm{A}}q_{\mathrm{A}}}^{ij} = {}^{\mathrm{B}}\mathcal{S}_{2,T_{\mathrm{BA}}(p_{\mathrm{A}})T_{\mathrm{BA}}(q_{\mathrm{A}})}^{ij}. \quad (18)
$$

The resulting matrix ${}^{\mathrm{A}}\mathcal{S}_2$ is still sparse but is no longer block diagonal, which results in the "mixing" of blocks related to the upper and lower sublattices and rise of specific moiré-induced physical effects.

Once we get scattering matrices of both sublayers in mutual basis A (or any other one), the total scattering matrix of the whole stack ${}^{\mathrm{A}}\mathcal{S} = {}^{\mathrm{A}}\mathcal{S}^1 \otimes {}^{\mathrm{A}}\mathcal{S}^2$ might be found via the well-known formulas [75] (from here on we omit the index A, implying that all the matrices are derived in the same basis):

$$
\mathcal{S}^{\mathrm{dd}} = \mathcal{S}_2^{\mathrm{dd}}(\hat{I} - \mathcal{S}_1^{\mathrm{du}}\mathcal{S}_2^{\mathrm{ud}})^{-1}\mathcal{S}_1^{\mathrm{dd}}, \quad (19)
$$

$$
\mathcal{S}^{\mathrm{du}} = \mathcal{S}_2^{\mathrm{du}} + \mathcal{S}_2^{\mathrm{dd}}(\hat{I} - \mathcal{S}_1^{\mathrm{du}}\mathcal{S}_2^{\mathrm{ud}})^{-1}\mathcal{S}_1^{\mathrm{du}}\mathcal{S}_2^{\mathrm{uu}}, \quad (20)
$$

$$
\mathcal{S}^{\mathrm{ud}} = \mathcal{S}_1^{\mathrm{ud}} + \mathcal{S}_1^{\mathrm{uu}}(\hat{I} - \mathcal{S}_2^{\mathrm{ud}}\mathcal{S}_1^{\mathrm{du}})^{-1}\mathcal{S}_2^{\mathrm{ud}}\mathcal{S}_1^{\mathrm{dd}}, \quad (21)
$$

$$
\mathcal{S}^{\mathrm{uu}} = \mathcal{S}_1^{\mathrm{uu}}(\hat{I} - \mathcal{S}_2^{\mathrm{ud}}\mathcal{S}_1^{\mathrm{du}})^{-1}\mathcal{S}_2^{\mathrm{uu}}, \quad (22)
$$

where the matrices are considered in terms of large $2N_gM_g \times 2N_gM_g$ blocks:

$$
\mathcal{S}(\omega, \mathbf{k}_\parallel) = \begin{pmatrix} \mathcal{S}^{\mathrm{dd}} & \mathcal{S}^{\mathrm{du}} \\ \mathcal{S}^{\mathrm{ud}} & \mathcal{S}^{\mathrm{uu}} \end{pmatrix}, \quad (23)
$$

$$
\mathcal{S}_1(\omega, \mathbf{k}_\parallel) = \begin{pmatrix} \mathcal{S}_1^{\mathrm{dd}} & \mathcal{S}_1^{\mathrm{du}} \\ \mathcal{S}_1^{\mathrm{ud}} & \mathcal{S}_1^{\mathrm{uu}} \end{pmatrix}, \quad (24)
$$

$$
\mathcal{S}_2(\omega, \mathbf{k}_\parallel) = \begin{pmatrix} \mathcal{S}_2^{\mathrm{dd}} & \mathcal{S}_2^{\mathrm{du}} \\ \mathcal{S}_2^{\mathrm{ud}} & \mathcal{S}_2^{\mathrm{uu}} \end{pmatrix}. \quad (25)
$$

Each of formulas (19)–(22) contains the inversion of the sparse matrices for which, to our knowledge, there are no effective specialized algorithms. In this way, since the time of the matrix inversion scales cubically with its size, the total computation time for the stack scattering matrix has the same cubic asymptote $\tau \propto N_g^3 M_g^3$ as the naive approach. Nevertheless, even the efficient calculation of each sublattice matrix, as we will show below, accelerates the whole procedure multiple times.

III. FILTRATION OF HARMONICS

In most practical cases, calculation of the moiré stack scattering matrix might be additionally boosted as well. If there is a thin, but finite, homogeneous gap layer of thickness H (see Fig. 1) between twisted metasurfaces, then additional physical-based simplification can be implemented. Indeed, high-$k_\parallel$ evanescent waves (requiring a large number of harmonics in the calculation to be accounted for) might be needed to accurately describe the optical properties of separate upper and lower lattices. Nevertheless, these harmonics decay in the gap in such a fast way that they make almost no contribution in the interaction of upper and lower sublayers. Therefore, it is easy to formulate the criterion for taking harmonics into account for the calculation of matrix combination:

$$
e^{-\mathrm{Im}[\sqrt{\varepsilon_{\mathrm{gl}}\omega^2/c^2 - (\mathbf{k}_\parallel + n\mathbf{G}^1 + m\mathbf{G}^2)^2}H]} > \Theta, \quad (26)
$$

where $\varepsilon_{\mathrm{gl}}$ is the permittivity of the gap layer and Θ is the cutoff level, which determines the tolerance of the fully converged results and should be in the range of 10^{-2}–10^{-10} for most of the structures. Harmonic filtering is schematically illustrated in Fig. 2(c). The fulfillment of the introduced condition results in throwing away a significant number of corresponding rows and columns from matrices $\mathbb{S}_1$ and $\mathbb{S}_2$ and a subsequent drastic increase in the calculation speed for Eqs. (19)–(22). Moreover, the number of remaining harmonics saturates rapidly, making the computation time of matrix combination almost constant as well. In this case, the asymptotic time scaling will be determined by the sublattices $\tau \propto \max(N_g^3 M_g, N_g M_g^3)$. If one is not satisfied with the Θ-limited precision, it is possible to reduce the cutoff level synchronously with the increase in the number of harmonics. Such approach would worsen the asymptotic behavior but guarantee the ultimate precision with a remaining great gain in speed.

It is important that despite the filtration, we still account for the near field of the metasurfaces and the potential coupling

of their guided modes by the near-field interaction. Crucially, even though high harmonics are not in demand in the last computational stage, accounting for the interaction between the sublayers, they are vital to obtaining the low-$\mathbf{k}_\parallel$ cores of the $\mathbb{S}_1$ and $\mathbb{S}_2$ matrices since sublattices might efficiently "mix" all the harmonics. Therefore, the number of harmonics $N_g M_g$ used to calculate $\mathbb{S}_1$ and $\mathbb{S}_2$ should be, in general, significantly larger than the number which fulfills condition (26).

In the case of zero or extremely small H, the filtering technique is not applicable and does not increase the calculation efficiency. However, this case corresponds to tightly bound lattices that form a true 2D crystal, and it is reasonable that the simplification based on the concept of complex independent structures connected via the limited number of channels is irrelevant.

Further development

Computational approaches presented in the previous sections provide a fast and efficient calculation of twisted moiré stack spectra, which will be demonstrated below. Nevertheless, the computations can be further improved, which might be vital in most complicated cases.

The most obvious improvement is associated with the filtration of harmonics. In most practical cases we keep a rather limited number of low-$\mathbf{k}_\parallel$ harmonics that lie in a circle defined by the cutoff level in Eq. (26). Without loss of generality, if we consider the upper lattice, then it becomes obvious that most of the chains of the harmonics [right column in Fig. 2(a)] are not related to the low $\mathbf{k}_\parallel$ in which we are interested. Therefore, the corresponding blocks of the scattering matrices can be excluded, which additionally improves the time calculation asymptote $\tau \propto \max(N_g^3, M_g^3)$. Such an approach requires a slightly more complicated procedure for the choice of the mutual basis and harmonics of individual lattices, which should account for the cutoff level. Nevertheless, this procedure is straightforward and might be easily realized in the spirit of the technique presented in this study. Potential interest in efficient calculations might be attracted by the choice of other alternative 2D harmonics sets that are not direct sums of any other 1D harmonics sets.

One more opportunity to improve the computations for the weakly coupled metasurfaces lies in a simplified accounting of their interaction. Indeed, in such cases it is most likely possible to develop some sort of perturbation theory. Apparently, it will be associated with substituting expressions with inversion of the matrices with series expansion [see Eqs. (19)–(22)]. Potentially, the use of only sparse matrix multiplication, which is a fast operation, might significantly boost the calculations. Nevertheless, this approach requires separate detailed consideration and rigorous study of its potential applicability.

Yet another acceleration can be applied for the hard-to-compute moiré superlattices of large moiré periods. As already discussed, similar sublattice superimposition results in the formation of a very dense reciprocal lattice, and according to the described procedure, one needs to calculate the blocks of matrices that connect very closely located chains of harmonics. Therefore, corresponding scattering matrices might be found not directly, but from the interpolation of precalculated matrices on a mesh in reciprocal space. Such

an approach not only strongly reduces the number of repeated calculations but also helps us to choose the optimum for the problem set of harmonics (not necessarily direct sum generated).

IV. PERFORMANCE

In the previous sections, we have proposed an effective computational approach and estimated its asymptotic time consumption. Nevertheless, it is important to observe the acceleration in practice. To do that, we have chosen one of the hardest-to-compute structures: the stack of two 1D plasmonic lattices in silica ($\varepsilon_{\text{SiO}_2} = 1.46^2$). Figure 4(a) indicates the dimensions of perpendicular gold lattices that are identical to each other. The optical properties of gold are described by Johnson and Christy's optical constants [76].

As an illustration, we consider the normal incidence of x-polarized 1200-nm light on the structure. Figures 4(b) and 4(c) show the dependence of the absorption and the calculation time, respectively, on the number of Fourier harmonics taken into account (we take $N_g = M_g$ for all the computations). The green line and circles show the application of the standard Fourier modal method (enhanced by Li's factorization rules [77,78]) to a 2D grating (straightforward approach) and act as reference values. One can see from Fig. 4(c) that on logarithmic axes, single-processor calculation time almost immediately goes to a straight line of almost constant slope, ≈ 2.5, which is slightly smaller than the theoretical asymptotic limit of 3. The last computed point corresponding to $47^2 = 2209$ Fourier harmonics takes approximately 600 s. Nevertheless, due to the peculiarities of the metal properties, the absorption value is still far from convergence even for as large a number of harmonics as 2209 (see Fig. 4).

The application of the techniques proposed in this paper allows us to accelerate the calculations significantly. For the zero cutoff level [yellow line and circles in Figs. 4(b) and 4(c)] there is no filtration of high-$\mathbf{k}_\parallel$ harmonics at all, which results in the same asymptotic time scaling [Fig. 4(c)] and identical absorption [Fig. 4(b)], which matches the standard FMM up to machine precision. Nevertheless, the optimal approach for calculating the sublayer scattering matrices makes the computations approximately 1 order of magnitude faster, which is clearly seen from the gap between the parallel green and yellow lines [Fig. 4(c)]. The reason is the number of the most asymptotically expensive mathematical operations is reduced approximately tenfold, which gives us the possibility to account for a much larger number of harmonics for the same computational time.

Nevertheless, even more promising results are demonstrated by the approximate method that filters out high Fourier harmonics in the stage of calculating the combination of sublayer scattering matrices. Even such a small cutoff level as $\Theta = 10^{-10}$ results in a total change in the computation time dependence [red line in Fig. 4(c)]. Indeed, while the number of harmonics is relatively small [all of them fit inside the dashed circle in Fig. 2(c)], none of them is ignored [in Fig. 4(c), the red and yellow lines coincide], but as soon as their number overcomes the threshold of approximately 670 harmonics, which can easily be estimated [some of the harmonics come out of the circle in Fig. 2(c)], the time to
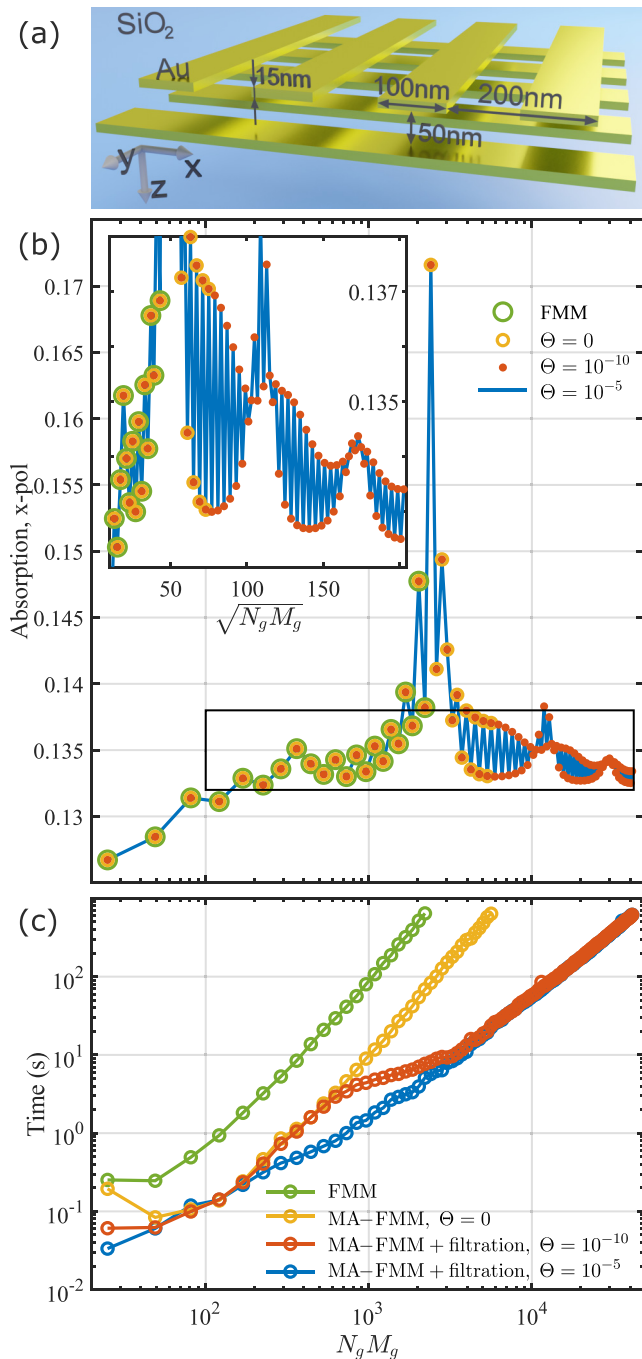
FIG. 4. Study of the computation convergence with the number of harmonics used to calculate the absorption of normally incident *x*-polarized light in the plasmonic stack depicted in (a). (b) shows the dependence of the absorption on the total number of harmonics taken into account in a logarithmic scale. The inset employs the linear scale for the square root of the harmonics to demonstrate the details of the oscillations near the expected limit. (c) shows the calculation time scaling with the number of harmonics for the different approaches. The green line and circles correspond to the reference FMM, and the yellow line and circles correspond to our approach without filtration, whereas red and blue ones correspond to different filtration cutoff levels.

compute the scattering matrix combination stops growing. This results in a bend in the graph line and a flattening of its asymptote, which is reached when the time required to

compute upper and lower sublayer scattering matrices dominates the their combination time. As shown before, theoretical estimation gives the quadratic scaling of the computation time $\tau \propto (N_g M_g)^2$ (for $N_g = M_g$), but in practice, we see a power of approximately 1.7. In this way, the harmonics filtration results in an additional strong acceleration of the computations, and moreover, this acceleration becomes greater as more harmonics are taken into account. It is also important that although the filtration-based approach is approximate, the computed absorption values match perfectly the previous results, and no significant deviation is seen [see Fig. 4(b)]. Therefore, the level of filtration-specified precision does not prevent obtaining almost the full convergence potentially.

A relatively high cutoff level of $\Theta = 10^{-5}$ (blue lines and circles) shifts the threshold of line bending to a much smaller number of harmonics, so that it is no longer distinguishable [Fig. 4(c)]. As seen from the graphs, this gives us a significant acceleration for the middle number of harmonics (300–3000), which can be the most practical in calculations of many structures. At the same time, the coincidence with the previous, accurate calculations is perfect, which proves the remaining high level of precision [Fig. 4(b)].

The optimal choice of the number of harmonics and the cutoff level significantly depends on the materials and geometry of the structure, physical effects observed in the considered frequency range, and, obviously, the desired precision. The most attention should be paid to achieving the convergence for $N_g M_g$ and θ, although the computational time is essential as well.

V. EXAMPLES

The high speed and precision of computations make it much easier to compute spectra of moiré metasurfaces. In particular, here, we explore the potential applications of the computational approach for the examples of the already discussed plasmonic lattices (twisted on different angles) and a membrane diamond photonic crystal slab.

A. Plasmonic crystal

Plasmonic crystals and inclusions of plasmonic nanoparticles in photonic crystal slabs are well known for their ability to localize light at the nanoscale and form hybrid high-Q collective resonances [29,33,79–95]. Without a doubt, they can become the basis for a variety of moiré superlattices as well.

The natural way to study the optical properties of the twisted plasmonic gratings is to consider isofrequency dispersion curves. In order to do that, we employ an auxiliary high-index optical prism ($\varepsilon_{prism} = 16$) at a small distance from the structure (see schemes in Fig. 5) and use it for excitation of the guided modes. The absorption maps for *p*-polarized 1200-nm light, which excites surface plasmons in plasmonic structures, are shown in Fig. 5. Figures 5(a) and 5(b) demonstrate that solitary lattices [constituents of the stacks considered further in panels (c)-(d)] support plasmons propagating along the gold sheets. Indeed, the longitudinally polarized surface waves that propagate along the structure almost do not feel the vertical walls of nanostrips and behave similarly
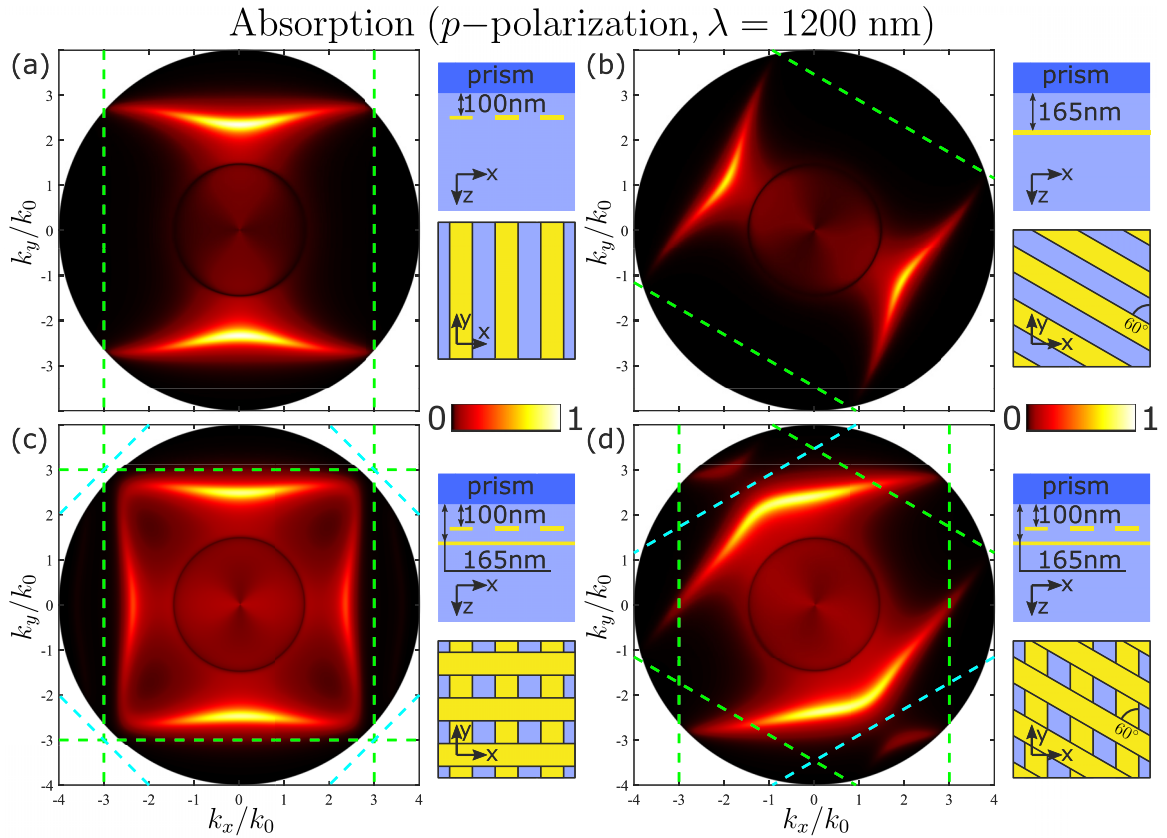
FIG. 5. Absorption maps of *p*-polarized 1200-nm-wavelength light in four sketched SiO$_2$-embedded plasmonic lattices illuminated through the prism (k_x/k_0 and k_y/k_0 are in-plain wave vector components normalized by the wave vector in vacuum $k_0 = \omega/c$; *x*-*y* projections show the bottom-up view, which is in accordance with other figures). (a) and (b) demonstrate the hyperboliclike behavior of plasmons in solitary lattices placed at different distances from the prism. (c) and (d) show the mode hybridization in stacks of (c) perpendicularly and (d) 60°-angle-crossed identical plasmonic lattices. Green dashed lines indicate the boundaries of the 1D lattices Brillouin zones, whereas the cyan lines are moiré-pattern-associated boundaries.

to plasmons in an infinite metal slab. At the same time, the plasmonic modes polarized perpendicularly to the strips face strong depolarization due to the subwavelength dimensions of the latter one. For this reason such modes are naturally associated with localized resonances that are observed for smaller wavelengths. The fact that at the considered wavelength plasmon waves can propagate in one direction but cannot propagate in the other one leads to concavity of its dispersion. An effective anisotropic medium cannot accurately describe these plasmons due to the proximity of the first Brillouin zone boundaries (green dashed lines) to the dispersion curves. Nevertheless, the dispersion curves demonstrate typical hyperboliclike behavior [96], which is widely spread in various nanophotonic applications [39]. It is worth noting that the modes of the structure located 100 nm from the prism [Fig. 5(a)] are obviously more strongly excited than those of the 165-nm-disposed structure [Fig. 5(b)] due to the decay of evanescent waves in the SiO$_2$ layer.

Hybridization of upper and lower lattice plasmons in a stack is able to change their dispersion significantly. Interestingly, even the interaction of perpendicularly crossed lattices leads to the formation of the closed squarelike dispersion curve [see Fig. 5(c)]. This effect is very similar to a topological transition in twisted graphene metasurfaces [39]

and probably can also be implemented for so-called field canalization [39,97]. Nevertheless, like in the solitary lattices [Figs. 5(a) and 5(b)], *x*-propagating plasmons are less pronounced than *y*-propagating ones, which is explained just by an asymmetric prism-assisted excitation.

Relative rotation of the lattices is a powerful tool to shape the dispersion in a desired way. The 60° angle between nanoribbons makes the first Brillouin zone (Wigner-Seitz cell) a regular hexagon [see Fig. 5(d)], whereas the structure remains C_2 symmetric. Two pairs of its boundaries (shown by green dashed lines) originate from the reciprocal lattices of separate 1D sublattices, whereas the cyan pair corresponds to a specific moiré-inspired effect associated with both sublattices. The interaction of lattices is most pronounced where the resonances of individual lattices intersect [see Figs. 5(a) and 5(b) for corresponding dispersions]. Indeed, we observe strong anticrossing of the surface plasmons near the cyan boundary of the Brillouin zone. Nevertheless, in this example, hybridization is mostly due to the interaction through the main harmonic. The lattice effect associated with the vicinity of the Brillouin zone boundary and corresponding interaction with Bragg-vector-coupled harmonics is very weak and does not significantly affect the behavior of the structure. The shape of the newly
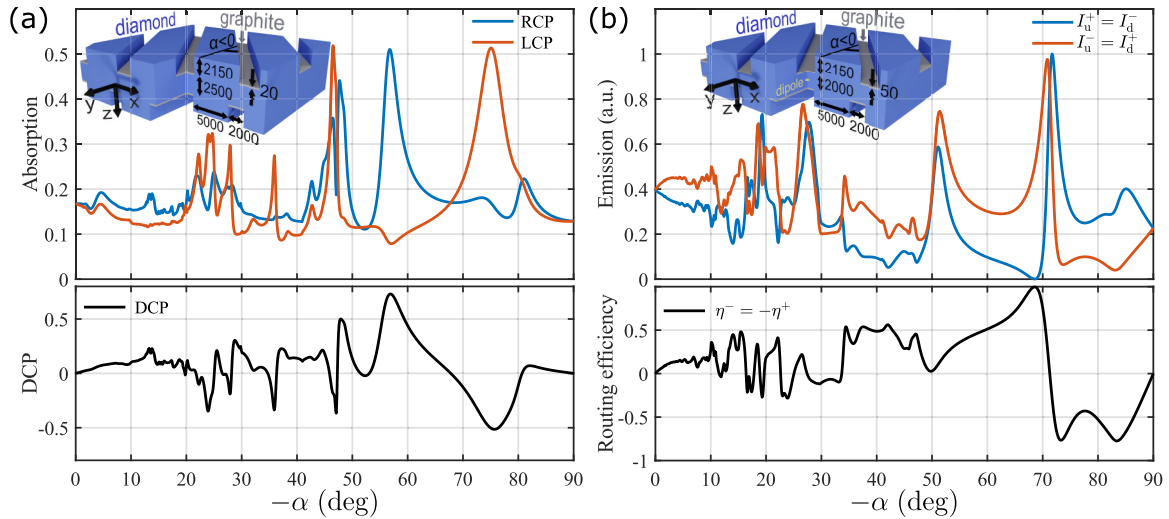
FIG. 6. (a) Absorption and (b) emission of 10-μm light from the twisted diamond photonic crystal slab with graphite inclusions (insets). (a) shows the absorption of the right- and left-handed circularly polarized light as well as the degree of circular polarization in absorption as a function of the rotation angle. (b) demonstrates the angle dependence of the upwards and downwards emission in the normal directions for the circularly polarized $\sigma^{\pm}$ dipoles. The bottom panel shows the routing efficiencies $\eta^{-} = -\eta^{+}$, which almost reach the ultimate unitary value.

formed dispersion curve is obviously determined by the original plasmons but strongly differs from them at the same time. Most importantly, dispersion becomes convex, which totally changes the behavior of the plasmon wave packet propagation.

B. Dielectric crystal

As an example of dielectric moiré structure, we explore the optical properties of diamond photonic crystal slabs (see the insets in Fig. 6) in the midinfrared frequency range ($\lambda = 10\,\mu$m). These structures are diamond membranes in which identical periodic series of grooves are cut from both sides. The bottom of the grooves is covered by a thin, several-dozen-nanometer layer of graphite, which is naturally formed during the direct laser writing [98]. The grooves are twisted on an angle α with respect to each other (the lower one is aligned with the y axis, $\beta = 0$, whereas the upper one is rotated by the angle $\alpha < 0$); the exact dimensions of the structures are indicated in Fig. 6. Diamond and graphite permittivities at 10-μm wavelength are $\varepsilon_d = 5.6581 + 0.0004i$ and $\varepsilon_g = 9.99 + 35.55i$, respectively [98].

The considered structures do not have any mirror symmetry in the general case, which makes them chiral and prospective for manipulating circularly polarized light. In this way, we illuminate the structure by the normally incident light of complementary circular polarizations and observe the absorption, which occurs predominantly (but not completely) in graphite. As we can see from Fig. 6(a), absorption strongly depends on the angle α; there are many resonances that are excited for different angles. We see that the degree of circular polarization (DCP), $(A_{\mathrm{RCP}} - A_{\mathrm{LCP}})/(A_{\mathrm{RCP}} + A_{\mathrm{LCP}})$, for the absorption reaches the high level of approximately 73% for an approximately 57° angle of rotation [see the bottom graph in Fig. 6(a)]. Even higher levels can be achieved with a thinner layer of graphite, but the finite physically meaningful thickness "blurs" the pure effect and limits its

maximal value. According to the Lorentz reciprocity principle, the shown effect means that the thermal emission of a 10-μm wavelength, which can be observed from the moiré structure, will be strongly circularly polarized in the normal direction. In this way, we can consider this structure a passive source of circularly polarized thermal emission, which might potentially be implemented in radiative heat transfer problems [45,58,60].

As for the angular dependence, it is clear that relatively large angles such as 50°–90° correspond to typical 2D lattices, which have periods comparable to each other in two directions. The periods of the structure, as well as its optical properties, slowly change with variation of the angle in this range, and therefore, the resonances are wide in terms of the angular width. Nevertheless, as we discussed before, one of the structure periods tends to infinity with an angle going to zero. This results in a large number of sharp resonances and Rayleigh anomalies that interchange with each other in the range of 15°–50°. At the same time, the efficiency of the high-harmonics excitation rapidly falls with decreasing angle, and as a result, the amplitude of the dense modulation in Fig. 6(a) becomes negligible for 0°–15°. It is important to emphasize once again that small angles of rotation potentially require us to take into account a huge number of harmonics, at least to cover open diffraction channels. Nevertheless, in practice, we observe that up to a high level of precision, the convergence is achieved even when not all the open channels are accounted for, which indirectly proves the weak contribution of the ignored harmonics to the properties of the whole structure. This effect paves the way for potential studies of even larger moiré period superlattices.

We consider the chiral structure, which has not only a z axis possessing a twofold rotation but also two other axes of the same kind lying in the x-y plane. Overall, the structure has D_2 point group symmetry, making it prospective for routing the radiation from the circularly polarized dipole emitter [99].

Indeed, let us consider a point dipole that is located in the structure according to the inset in Fig. 6(b), in the middle of each of the graphite strips (in terms of the x-y plane projection) and in the center of the slab (in terms of the z coordinate). We denote the dipoles of complementary circular polarizations $\mathbf{P}^{\pm} = [1, \pm i, 0]^{\mathrm{T}}$ as $\sigma^{\pm}$, respectively. In this way, due to the symmetry of the structure, the intensity of light emitted upwards at a normal angle by the σ^+ dipole I_u^+ is equal to the intensity of the σ^- dipole downwards emission, $I_d^- = I_u^+$. The same relation is valid for the complementary quantities, $I_u^- = I_d^+$. This peculiarity simplifies the route of $\sigma^{\pm}$ dipole emission to opposite directions. If we manage to nullify the downwards emission of the σ^- dipole $I_d^- = 0$, the upwards emission of the σ^+ dipole would automatically be zero as well, $I_u^+ = 0$, which means that each dipole would radiate in its own direction. Such a routing effect in the D_4-symmetric structure was already studied in detail in our previous paper [99].

It is convenient to evaluate the emission directivity numerically via the efficiencies $\eta^{\pm} = \frac{I_u^{\pm} - I_d^{\pm}}{I_u^{\pm} + I_d^{\pm}}$, which are connected to each other, and $\eta^+ = -\eta^-$. The accurate choice of the geometric parameters allowed us to achieve almost perfect routing (more than 99.5% efficiency) for an approximately $68°$ angle of rotation [Fig. 6(b)]. It is clear from the upper graph in Fig. 6(b) that the strongest effect corresponds to the nullification of the emission in one of the directions due to the Fano line shape of the resonance (blue line). In principle, the structure might be optimized to demonstrate this effect for narrow, small-angle resonances that are observed in emission as well.

VI. CONCLUSION

In this paper, we have proposed a moiré-adapted Fourier modal method to consider twisted 1D lattices that form moiré patterns. We have demonstrated the possibility of speeding up the computations by 1 to 3 or more orders of magnitude depending on the number of harmonics without a noticeable decrease in the accuracy. Such an approach paves the way for rigorous study of mode hybridization in twisted photonic crystals slabs and the potential design of optical devices based on them. As an example, we have demonstrated the tuning of plasmonic modes dispersion in a stack of plasmonic lattices. Also, the utilization of the diamond photonic crystal slab for circularly polarized thermal emission in the midinfrared range and emission routing from the circularly polarized dipole source have been shown.

ACKNOWLEDGMENTS

[1] S. Kishimoto, M. Egashira, and N. Shinya, Microcreep deformation measurements by a moiré method using electron beam lithography and electron beam scan, Opt. Eng. **32**, 522 (1993).

[2] D. Post, The moiré grid-analyzer method for strain analysis, Exp. Mech. **5**, 368 (1965).

[3] F.-P. Chiang, Moiré methods of strain analysis, Exp. Mech. **19**, 290 (1979).

[4] J. K. Drinkwater, B. W. Holmes, and K. A. Jones, Development and applications of diffractive optical security devices for banknotes and high value documents, in *Optical Security and Counterfeit Deterrence Techniques III*, Vol. 3973, edited by R. L. van Renesse and W. A. Vliegenthart (SPIE, 2000), pp. 66–77.

[5] M. King and D. Berry, Photolithographic mask alignment using moiré techniques, Appl. Opt. **11**, 2455 (1972).

[6] M. Mühlberger, I. Bergmair, W. Schwinger, M. Gmainer, R. Schöftner, T. Glinsner, C. Hasenfuß, K. Hingerl, M. Vogler, H. Schmidt, and E. B. Kley, A moiré method for high accuracy alignment in nanoimprint lithography, Microelectron. Eng. **84**, 925 (2007).

[7] N. Li, W. Wu, and S. Y. Chou, Sub-20-nm alignment in nanoimprint lithography using moire fringe, Nano Lett. **6**, 2626 (2006).

[8] R. Z. Wang and S. Weiner, Strain-structure relations in human teeth using moire fringes, J. Biomech. **31**, 135 (1997).

[9] Z. Wu, G. Kelp, M. N. Yogeesh, W. Li, K. M. McNicholas, A. Briggs, B. B. Rajeeva, D. Akinwande, S. R. Bank, G. Shvets *et al.*, Dual-band moiré metasurface patches for multifunctional biomedical applications, Nanoscale **8**, 18461 (2016).

[10] R. Sharma *et al.*, Structural and electronic transport properties of fluorographene directly grown on silicates for possible biosensor applications, ACS Appl. Nano Mater. **3**, 5399 (2020).

[11] S. Zhu, H. Li, M. Yang, and S. W. Pang, Highly sensitive detection of exosomes by 3D plasmonic photonic crystal biosensor, Nanoscale **10**, 19927 (2018).

[12] X. Zhang, E. Dalsgaard, S. Liu, H. Lai, and J. Chen, Concealed holographic coding for security applications by using a moiré technique, Appl. Opt. **36**, 8096 (1997).

[13] V. J. Cadarso, S. Chosson, K. Sidler, R. D. Hersch, and J. Brugger, High-resolution 1D moirés as counterfeit security features, Light: Sci. Appl. **2**, e86 (2013).

[14] A. Aggarwal, S. K. Kaura, D. Chhachhia, and A. Sharma, Concealed moiré pattern encoded security holograms readable by a key hologram, Opt. Laser Technol. **38**, 117 (2006).

[15] I. Amidror, S. Chosson, and R. D. Hersch, Moiré methods for the protection of documents and products: A short survey, J. Phys.: Conf. Ser. **77**, 012001 (2007).

[16] Z. Wu and Y. Zheng, Moiré metamaterials and metasurfaces, Adv. Opt. Mater. **6**, 1701057 (2018).

[17] H. Miao, A. Panna, A. A. Gomella, E. E. Bennett, S. Znati, L. Chen, and H. Wen, A universal moiré effect and application in X-ray phase-contrast imaging, Nat. Phys. **12**, 830 (2016).

[18] L. Balents, C. R. Dean, D. K. Efetov, and A. F. Young, Superconductivity and strong correlations in moiré flat bands, Nat. Phys. **16**, 725 (2020).

[19] G. Chen, A. L. Sharpe, P. Gallagher, I. T. Rosen, E. J. Fox, L. Jiang, B. Lyu, H. Li, K. Watanabe, T. Taniguchi, J. Jung, Z. Shi,

D. Goldhaber-Gordon, Y. Zhang, and F. Wang, Signatures of tunable superconductivity in a trilayer graphene moiré superlattice, Nature (London) **572**, 215 (2019).

[20] Y. Cao, V. Fatemi, S. Fang, K. Watanabe, T. Taniguchi, E. Kaxiras, and P. Jarillo-Herrero, Unconventional superconductivity in magic-angle graphene superlattices, Nature (London) **556**, 43 (2018).

[21] J. H. Pixley and E. Y. Andrei, Ferromagnetism in magic-angle graphene, Science **365**, 543 (2019).

[22] A. L. Sharpe, E. J. Fox, A. W. Barnard, J. Finney, K. Watanabe, T. Taniguchi, M. A. Kastner, and D. Goldhaber-Gordon, Emergent ferromagnetism near three-quarters filling in twisted bilayer graphene, Science **365**, 605 (2019).

[23] G. Chen, A. L. Sharpe, E. J. Fox, Y. H. Zhang, S. Wang, L. Jiang, B. Lyu, H. Li, K. Watanabe, T. Taniguchi, Z. Shi, T. Senthil, D. Goldhaber-Gordon, Y. Zhang, and F. Wang, Tunable correlated Chern insulator and ferromagnetism in a moiré superlattice, Nature (London) **579**, 56 (2020).

[24] C. Repellin, Z. Dong, Y. H. Zhang, and T. Senthil, Ferromagnetism in Narrow Bands of Moiré Superlattices, Phys. Rev. Lett. **124**, 187601 (2020).

[25] G. Li, A. Luican, J. M. Lopes Dos Santos, A. H. Castro Neto, A. Reina, J. Kong, and E. Y. Andrei, Observation of Van Hove singularities in twisted graphene layers, Nat. Phys. **6**, 109 (2010).

[26] Y. Jiang, X. Lai, K. Watanabe, T. Taniguchi, K. Haule, J. Mao, and E. Y. Andrei, Charge order and broken rotational symmetry in magic-angle twisted bilayer graphene, Nature (London) **573**, 91 (2019).

[27] E. Y. Andrei, D. K. Efetov, P. Jarillo-Herrero, A. H. MacDonald, K. F. Mak, T. Senthil, E. Tutuc, A. Yazdani, and A. F. Young, The marvels of moiré materials, Nat. Rev. Materials **6**, 201 (2021).

[28] K. Slagle and L. Fu, Charge transfer excitations, pair density waves, and superconductivity in moiré materials, Phys. Rev. B **102**, 235423 (2020).

[29] I. M. Fradkin, S. A. Dyakov, and N. A. Gippius, Thickness-Independent Narrow Resonance in a Stack of Plasmonic Lattices, Phys. Rev. Appl. **14**, 054030 (2020).

[30] D. Becerril, G. Pirruccio, and C. Noguez, Optical band engineering via vertical stacking of honeycomb plasmonic lattices, Phys. Rev. B **103**, 195412 (2021).

[31] S. Murai, K. Agata, and K. Tanaka, Photoluminescence from an emitter layer sandwiched between the stack of metasurfaces, J. Appl. Phys. **129**, 183101 (2021).

[32] S. Chen, Y. Zhang, Z. Li, H. Cheng, and J. Tian, Empowered layer effects and prominent properties in few-layer metasurfaces, Adv. Opt. Mater. **7**, 1801477 (2019).

[33] N. A. Gippius, T. Weiss, S. G. Tikhodeev, and H. Giessen, Resonant mode coupling of optical resonances in stacked nanostructures, Opt. Express **18**, 7569 (2010).

[34] X.-D. Chen, X.-T. He, and J.-W. Dong, All-dielectric layered photonic topological insulators, Laser Photonics Rev. **13**, 1900091 (2019).

[35] A. Berkhout and A. F. Koenderink, A simple transfer-matrix model for metasurface multilayer systems, Nanophotonics **9**, 3985 (2020).

[36] A. Berkhout and A. F. Koenderink, Perfect absorption and phase singularities in plasmon antenna array etalons, ACS Photonics **6**, 2917 (2019).

[37] A. Berkhout, T. A. Wolterink, and A. F. Koenderink, Strong

coupling to generate complex birefringence: Metasurface in the middle etalons, ACS Photonics **7**, 2799 (2020).

[38] V. Gerasimov, A. Ershov, R. Bikbaev, I. Rasskazov, I. Timofeev, S. Polyutov, and S. Karpov, Engineering mode hybridization in regular arrays of plasmonic nanoparticles embedded in 1D photonic crystal, J. Quant. Spectrosc. Radiat. Transfer **224**, 303 (2019).

[39] G. Hu, A. Krasnok, Y. Mazor, C.-W. Qiu, and A. Alù, Moiré hyperbolic metasurfaces, Nano Lett. **20**, 3217 (2020).

[40] G. Hu, Q. Ou, G. Si, Y. Wu, J. Wu, Z. Dai, A. Krasnok, Y. Mazor, Q. Zhang, Q. Bao *et al.*, Topological polaritons and photonic magic angles in twisted α-MoO$_3$ bilayers, Nature (London) **582**, 209 (2020).

[41] Z. Zheng, F. Sun, W. Huang, J. Jiang, R. Zhan, Y. Ke, H. Chen, and S. Deng, Phonon polaritons in twisted double-layers of hyperbolic van der Waals crystals, Nano Lett. **20**, 5301 (2020).

[42] J. Duan, N. Capote-Robayna, J. Taboada-Gutiérrez, G. Álvarez-Pérez, I. Prieto, J. Martín-Sánchez, A. Y. Nikitin, and P. Alonso-González, Twisted nano-optics: manipulating light at the nanoscale with twisted phonon polaritonic slabs, Nano Lett. **20**, 5323 (2020).

[43] M. Chen, X. Lin, T. H. Dinh, Z. Zheng, J. Shen, Q. Ma, H. Chen, P. Jarillo-Herrero, and S. Dai, Configurable phonon polaritons in twisted α-MoO$_3$, Nat. Mater. **19**, 1307 (2020).

[44] O. V. Kotov and Y. E. Lozovik, Hyperbolic hybrid waves and optical topological transitions in few-layer anisotropic metasurfaces, Phys. Rev. B **100**, 165424 (2019).

[45] C.-L. Zhou, X.-H. Wu, Y. Zhang, H.-L. Yi, and M. Antezza, Polariton topological transition effects on radiative heat transfer, Phys. Rev. B **103**, 155404 (2021).

[46] P. Wang, Y. Zheng, X. Chen, C. Huang, Y. V. Kartashov, L. Torner, V. V. Konotop, and F. Ye, Localization and delocalization of light in photonic moiré lattices, Nature (London) **577**, 42 (2020).

[47] M. Martí-Sabaté and D. Torrent, Dipolar Localization of Waves in Twisted Phononic Crystal Plates, Phys. Rev. Appl. **15**, L011001 (2021).

[48] J. Zeng, Y. Hu, X. Zhang, S. Fu, H. Yin, Z. Li, and Z. Chen, Localization-to-delocalization transition of light in frequency-tuned photonic moiré lattices, Opt. Express **29**, 25388 (2021).

[49] O. Aftenieva, M. Schnepf, B. Mehlhorn, and T. A. König, Tunable circular dichroism by photoluminescent moiré gratings, Adv. Opt. Mater. **9**, 2001280 (2021).

[50] Z. Wu, X. Chen, M. Wang, J. Dong, and Y. Zheng, High-performance ultrathin active chiral metamaterials, ACS Nano **12**, 5030 (2018).

[51] Y. Zhao, M. Belkin, and A. Alù, Twisted optical metamaterials for planarized ultrathin broadband circular polarizers, Nat. Commun. **3**, 870 (2012).

[52] R. Messina, A. Noto, B. Guizal, and M. Antezza, Radiative heat transfer between metallic gratings using fourier modal method with adaptive spatial resolution, Phys. Rev. B **95**, 125404 (2017).

[53] Y. H. Kan, C. Y. Zhao, and Z. M. Zhang, Near-field radiative heat transfer in three-body systems with periodic structures, Phys. Rev. B **99**, 035433 (2019).

[54] J. Dai, S. A. Dyakov, and M. Yan, Enhanced near-field radiative heat transfer between corrugated metal plates: Role of spoof surface plasmon polaritons, Phys. Rev. B **92**, 035419 (2015).

[55] V. Fernández-Hurtado, F. J. García-Vidal, S. Fan, and J. C.

Cuevas, Enhancing Near-Field Radiative Heat Transfer with Si-Based Metasurfaces, Phys. Rev. Lett. **118**, 203901 (2017).

[56] J. Dai, S. A. Dyakov, S. I. Bozhevolnyi, and M. Yan, Near-field radiative heat transfer between metasurfaces: A full-wave study based on two-dimensional grooved metal plates, Phys. Rev. B **94**, 125431 (2016).

[57] J. Dai, S. A. Dyakov, and M. Yan, Radiative heat transfer between two dielectric-filled metal gratings, Phys. Rev. B **93**, 155403 (2016).

[58] M. Luo, J. Zhao, and M. Antezza, Near-field radiative heat transfer between twisted nanoparticle gratings, Appl. Phys. Lett. **117**, 053901 (2020).

[59] S.-A. Biehs, F. S. Rosa, and P. Ben-Abdallah, Modulation of near-field heat transfer between two gratings, Appl. Phys. Lett. **98**, 243102 (2011).

[60] J. Peng, G. Tang, L. Wang, R. Macêdo, H. Chen, and J. Ren, Twist-induced near-field thermal switch using nonreciprocal surface magnon-polaritons, ACS Photon. **8**, 2183 (2021).

[61] C. Guo, Y. Guo, B. Lou, and S. Fan, Wide wavelength-tunable narrow-band thermal radiation from moiré patterns, Appl. Phys. Lett. **118**, 131111 (2021).

[62] A. Ushkov, I. Verrier, T. Kampfe, and Y. Jourlin, Subwavelength diffraction gratings with macroscopic moiré patterns generated via laser interference lithography, Opt. Express **28**, 16453 (2020).

[63] C. Menzel, J. Sperrhake, and T. Pertsch, Efficient treatment of stacked metasurfaces for optimizing and enhancing the range of accessible optical functionalities, Phys. Rev. A **93**, 063832 (2016).

[64] A. N. Askarpour, Y. Zhao, and A. Alù, Wave propagation in twisted metamaterials, Phys. Rev. B **90**, 054305 (2014).

[65] X. Romain, Study of polarization of light through a stack of metallic metamaterials, Ph.D. thesis, Université Bourgogne Franche-Comté, 2018.

[66] J. Sperrhake, M. Falkner, S. Fasold, T. Kaiser, and T. Pertsch, Equivalence of reflection paths of light and Feynman paths in stacked metasurfaces, Phys. Rev. B **102**, 245108 (2020).

[67] J. Sperrhake, M. Decker, M. Falkner, S. Fasold, T. Kaiser, I. Staude, and T. Pertsch, Analyzing the polarization response of a chiral metasurface stack by semi-analytic modeling, Opt. Express **27**, 1236 (2019).

[68] X. Romain, F. I. Baida, and P. Boyer, Spectrally tunable linear polarization rotation using stacked metallic metamaterials, J. Opt. **19**, 085102 (2017).

[69] X. Romain, F. Baida, and P. Boyer, Extended Malus law with terahertz metallic metamaterials for sensitive detection with giant tunable quality factor, Phys. Rev. B **94**, 045407 (2016).

[70] B. Lou, N. Zhao, M. Minkov, C. Guo, M. Orenstein, and S. Fan, Theory for Twisted Bilayer Photonic Crystal Slabs, Phys. Rev. Lett. **126**, 136101 (2021).

[71] D. X. Nguyen, X. Letartre, E. Drouard, P. Viktorovitch, H. C. Nguyen, and H. S. Nguyen, Magic configurations in moiré superlattice of bilayer photonic crystal: Almost-perfect flatbands and unconventional localization, arXiv:2104.12774.

[72] H. Tang, F. Du, S. Carr, C. DeVault, O. Mello, and E. Mazur, Modeling the optical properties of twisted bilayer photonic crystals, Light: Science & Applications **10**, 157 (2021).

[73] S. G. Tikhodeev, A. L. Yablonskii, E. A. Muljarov, N. A. Gippius, and T. Ishihara, Quasiguided modes and optical properties of photonic crystal slabs, Phys. Rev. B **66**, 045102 (2002).

[74] M. Moharam, E. B. Grann, D. A. Pommet, and T. Gaylord, Formulation for stable and efficient implementation of the rigorous coupled-wave analysis of binary gratings, J. Opt. Soc. Am. A **12**, 1068 (1995).

[75] T. Weiss, N. A. Gippius, S. G. Tikhodeev, G. Granet, and H. Giessen, Efficient calculation of the optical properties of stacked metamaterials with a Fourier modal method, J. Opt. A **11**, 114019 (2009).

[76] P. B. Johnson and R. W. Christy, Optical constants of the noble metals, Phys. Rev. B **6**, 4370 (1972).

[77] L. Li, New formulation of the fourier modal method for crossed surface-relief gratings, J. Opt. Soc. Am. A **14**, 2758 (1997).

[78] L. Li, Use of Fourier series in the analysis of discontinuous periodic structures, J. Opt. Soc. Am. A **13**, 1870 (1996).

[79] I. M. Fradkin, S. A. Dyakov, and N. A. Gippius, Fourier modal method for the description of nanoparticle lattices in the dipole approximation, Phys. Rev. B **99**, 075310 (2019).

[80] I. M. Fradkin, S. A. Dyakov, and N. A. Gippius, Nanoparticle lattices with bases: Fourier modal method and dipole approximation, Phys. Rev. B **102**, 045432 (2020).

[81] L. Zundel, A. May, and A. Manjavacas, Lattice resonances induced by periodic vacancies in arrays of nanoparticles, ACS Photonics **8**, 360 (2021).

[82] A. Cuartero-González, S. Sanders, L. Zundel, A. I. Fernández-Domínguez, and A. Manjavacas, Super- and subradiant lattice resonances in bipartite nanoparticle arrays, ACS Nano **14**, 11876 (2020).

[83] S. Baur, S. Sanders, and A. Manjavacas, Hybridization of lattice resonances, ACS Nano **12**, 1618 (2018).

[84] A. D. Utyushev, V. I. Zakomirnyi, and I. L. Rasskazov, Collective lattice resonances: Plasmonics and beyond, Rev. Phys. **6**, 100051 (2021).

[85] R. Guo, T. K. Hakala, and P. Törmä, Geometry dependence of surface lattice resonances in plasmonic nanoparticle arrays, Phys. Rev. B **95**, 155423 (2017).

[86] M. S. Bin-Alam, O. Reshef, Y. Mamchur, M. Z. Alam, G. Carlow, J. Upham, B. T. Sullivan, J.-M. Ménard, M. J. Huttunen, R. W. Boyd *et al.*, Ultra-high-q resonances in plasmonic metasurfaces, Nat. Commun. **12**, 974 (2021).

[87] O. Reshef, M. Saad-Bin-Alam, M. J. Huttunen, G. Carlow, B. T. Sullivan, J.-M. Ménard, K. Dolgaleva, and R. W. Boyd, Multiresonant high-q plasmonic metasurfaces, Nano Lett. **19**, 6429 (2019).

[88] O. Y. Yermakov, D. V. Permyakov, F. V. Porubaev, P. A. Dmitriev, A. K. Samusev, I. V. Iorsh, R. Malureanu, A. V. Lavrinenko, and A. A. Bogdanov, Effective surface conductivity of optical hyperbolic metasurfaces: From far-field characterization to surface wave analysis, Sci. Rep. **8**, 14135 (2018).

[89] A. Samusev, I. Mukhin, R. Malureanu, O. Takayama, D. V. Permyakov, I. S. Sinev, D. Baranov, O. Yermakov, I. V. Iorsh, A. A. Bogdanov *et al.*, Polarization-resolved characterization of plasmon waves supported by an anisotropic metasurface, Opt. Express **25**, 32631 (2017).

[90] R. Kolkowski and A. F. Koenderink, Lattice resonances in optical metasurfaces with gain and loss, Proc. IEEE **108**, 795 (2020).

[91] A. Vaskin, R. Kolkowski, A. F. Koenderink, and I. Staude, Light-emitting metasurfaces, Nanophotonics **8**, 1151 (2019).

[92] A. S. Kostyukov, I. L. Rasskazov, V. S. Gerasimov, S. P. Polyutov, S. V. Karpov, and A. E. Ershov, Multipolar lattice resonances in plasmonic finite-size metasurfaces, Photonics **8**, 109 (2021).

[93] V. S. Gerasimov, A. E. Ershov, R. G. Bikbaev, I. L. Rasskazov, I. L. Isaev, P. N. Semina, A. S. Kostyukov, V. I. Zakomirnyi, S. P. Polyutov, and S. V. Karpov, Plasmonic lattice Kerker effect in ultraviolet-visible spectral range, Phys. Rev. B **103**, 035402 (2021).

[94] R. Guo, M. Nečada, T. K. Hakala, A. I. Väkeväinen, and P. Törmä, Lasing at *K* Points of a Honeycomb Plasmonic Lattice, Phys. Rev. Lett. **122**, 013901 (2019).

[95] M. Nečada and P. Törmä, Multiple-scattering t-matrix simulations for nanophotonics: Symmetries and periodic lattices, Commun. Comput. Phys. **30**, 357 (2021).

[96] O. Y. Yermakov, A. I. Ovcharenko, M. Song, A. A. Bogdanov, I. V. Iorsh, and Y. S. Kivshar, Hybrid waves localized at hyperbolic metasurfaces, Phys. Rev. B **91**, 235423 (2015).

[97] P. A. Belov, C. R. Simovski, and P. Ikonen, Canalization of subwavelength images by electromagnetic crystals, Phys. Rev. B **71**, 193105 (2005).

[98] M. S. Komlenok, S. G. Tikhodeev, A. A. Khomich, S. P. Lebedev, G. A. Komandin, and V. I. Konov, Optical properties of laser-modified diamond: From visible to microwave range, Quantum Electron. **49**, 672 (2019).

[99] S. A. Dyakov, N. A. Gippius, I. M. Fradkin, and S. G. Tikhodeev, Vertical Routing of Spinning-Dipole Radiation from a Chiral Metasurface, Phys. Rev. Appl. **14**, 024090 (2020).